International Journal of Rock Mechanics & Mining Sciences 130 (2020) 104315

Contents lists available at ScienceDirect

International Journal of Rock Mechanics and Mining Sciences

journal homepage: http://www.elsevier.com/locate/ijrmms

Coupled numerical approach combining X-FEM and the embedded discrete fracture method for the fluid-driven fracture propagation process in porous media

Cong Wang [a,b], Zhaoqin Huang [c,*], Yu-Shu Wu [a,**]

[a] Colorado School of Mines, Golden, United States
[b] Saudi Aramco, Dhahran, Saudi Arabia
[c] China University of Petroleum(Huadong), Qingdao, China

A B S T R A C T

A coupled simulation strategy combining the embedded discrete fracture method (EDFM) and the extended finite element method (X-FEM) is developed to simulate the fluid driven fracture propagation process in porous media. This physical process includes three strong coupling mechanics: fluid flow in fractures and porous media, solid deformation with fractures, and fracture propagations. The EDFM and X-FEM are used to simulate fracture-related fluid mechanics and solid mechanics, respectively, with information exchanged under the iterative numerical coupling scheme. Mathematical equations on how to link these independent modules as well as numerical techniques on how to accelerate the coupling convergence rate are discussed in detail.

Both X-FEM and EDFM avoid the cumbersome construction of unstructured grids to capture fracture paths and also avoid the remeshing for the fracture growth. They are first validated via benchmark problems individually and then are coupled to simulate fracture propagation problems in two dimensions and in three dimensions. Simulated multiphysics fields meet understandings qualitatively, and simulated fracture parameters (length, width and net pressure) match with analytical solutions quantitatively.

1. Introduction

The fluid-driven fracture propagation in porous media is a fundamental process to many applications in petroleum and mining engineering, such as hydraulic fracturing, produced water reinjection, borehole integrity, and drill cuttings reinjection. Quantitative evaluations of relevant fracture parameters are essential for the design analysis of these engineerings. However, modeling such a process is not an easy task because at least three strong coupling mechanics (Fig. 1) need to be accounted for: (1) fluid flow in fractures and porous media, (2) solid deformation, and (3) fracture propagations.[1] These three mechanics have entirely different natures and are governed by equations with different forms.

The pioneering contributors tried solving these coupled non-linear integral-differential equations by an analytical approach. Several classic fracturing models (PKN, KGD and Penny-shaped fracture model) were developed.[2–6] With some strong assumptions of simple geometry, these analytical solutions can capture the critical physics in this process, which contributes significantly to understanding the mechanism and physical effects of parameters in these equations. However, these analytical solutions have limitations to solving complex fracture problems, both physically and geometrically.

Later on, some pseudo-3D numerical tools were developed to simulate complex geometry problems with various finite element-based methods.[7–9] These tools were able to give more realistic estimates of fracture geometry/dimensions and thus achieved great success for conventional reservoirs. However, in the majority of available models, flow and solid deformation governing equations are oversimplified for the unconventional reservoirs. The rock elastic behaviors in these numerical models are described by a singular integral equation relating the fracture opening to the traction.[10] This equation was derived by assuming an infinite homogeneous three-dimensional elastic body, which has limited applications for layered strata characterized by different mechanical properties and/or in-situ stresses.

$$\frac{G}{4\pi(1-\nu)}\int_{\Omega}\left[\frac{\partial}{\partial x}\left(\frac{1}{r}\right)\frac{\partial w}{\partial x'}+\frac{\partial}{\partial y}\left(\frac{1}{r}\right)\frac{\partial w}{\partial y'}\right]dx'dy'=T(x,y) \tag{1}$$

where $r=[(x-x')^2+(y-y')^2]^{1/2}$, and $T(x,y)$ is the normal traction on the fracture surface at local (x, y), w is the fracture width; G is the shear

* Corresponding author.
** Corresponding author.
E-mail addresses: huangzhqin@upc.edu.cn (Z. Huang), ysw@mines.edu (Y.-S. Wu).

https://doi.org/10.1016/j.ijrmms.2020.104315
Received 24 December 2019; Received in revised form 26 March 2020; Accepted 27 March 2020
Available online 20 April 2020
1365-1609/© 2020 Elsevier Ltd. All rights reserved.

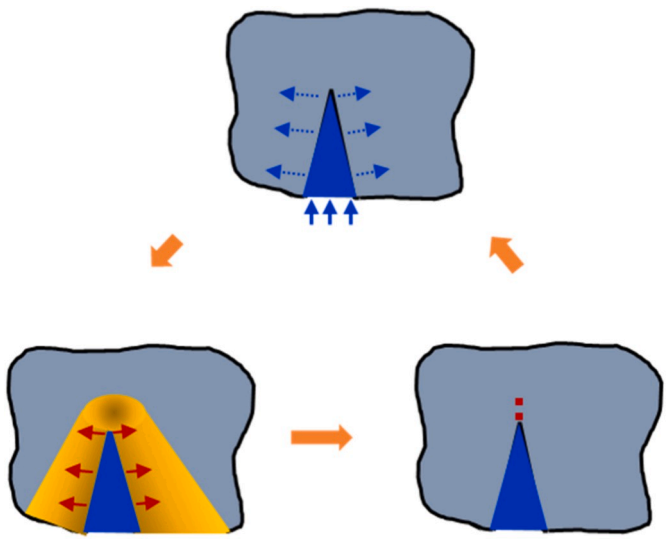

Fig. 1. Three strong coupling processes during the fluid-driven fracture propagations in porous media.

modulus; ν is Poisson's ratio of the material, and Ω is the fracture surface.

Fluid leakoff rate through fracture surfaces into the porous media in these numerical tools is quantified by[11]:

$$q_l = \frac{2c_l}{\sqrt{t - \tau(x, y)}} \tag{2}$$

where constant c_l is an empirical fluid leak-off coefficient and $\tau(x, y)$ is the time at which the fluid leak-off begins at location (x, y) on the fracture surface. This leak-off equation is derived by assuming a steady-state one-dimensional fluid flow, which has limitations for **low-perm** reservoirs with two following considerations. First, the transient-state flow may last long when the permeability is extremely low. And second, the pressure interference from nearby fractures is inevitable for complex fracture networks.

The finite element method (FEM)[12–15] and the discrete fracture method (DFM) based on the finite volume method (FVM)[16,17] provide a more general solution for handling fracture-related solid- and fluid-mechanics, respectively. In these two methods, fractures are represented by one or one set of small-size grids which conform to the fracture paths. Fluid and solid mechanics behaviors are captured by assigning these grids with fracture-related properties. However, developing these numerical models is challenging, with the following considerations. First, the mesh needs to be built in a way that the grid edges/faces coincide with all fracture surfaces, which requires the deployment of unstructured grids. Constructing such meshes is cumbersome especially for three-dimensional problems; second, in the finite element method, quadratic shape functions instead of linear shape functions are needed for the fracture tip grids to approximate the stress tip singularity; and third, remeshing is required at each time step for the fracture growth simulation.

The embedded discrete fracture method[18–21] and the extended finite element method[22,23] are two modeling techniques which extend the FEM and the DFM, respectively. Their basic ideas are both utilizing analytical-solution based approximations with geometrical preprocessing to account for mechanic interactions between fractures and local matrix blocks. In this way, three shortcomings regarding the FEM and DFM, as discussed above (cumbersome unstructured gridding, complicated fracture-tip shape functions, and remeshing for dynamic fractures), can be alleviated. In the EDFM, fractures are conceptualized to be virtually embedded into nearby matrix grid blocks by treating the fractures as single or several additional computational volume elements. In the X-FEM, the near fracture area is enriched by two additional groups of virtual nodes to incorporate both discontinuous fields and the near-tip asymptotic fields. A few recent efforts have been reported towards the development of these two numerical algorithms, mainly aiming for their improvement on accuracy, geometrical versatility and numerical robustness. Wang discussed the computational geometry issues regarding the 3D-EDFM as fractures in realistic engineering cases cannot simply be represented in two dimensions or 2.5 dimensions.[21] Hui et al. introduced three types of geometrical partitioning for complicated fracture-matrix topological characteristics.[25] The developed EDFM is applied for simulating fluid flow and heat transfer in unconventional oil & gas reservoirs as well as hot dry rock geothermal reservoirs.[21,24] Wang introduced a novel local mesh refinement approach with variable-node hexahedron elements for calculating stress intensity factors of straight and curved planar cracks.[26] Agathos et al. studied the stable 3D X-FEM vector level sets for non-planar 3D cracks.[27]

These novel discrete fracture methods enable us to conduct an analysis on the fluid-driven fracture propagation process. Lecampion investigated how to consider the presence of internal pressure inside the fracture.[28] Pan et al. coupled the TOUGH2 and rock discontinuous cellular automation (RDCA) to simulate the fluid flow and geomechanics coupling in subsurface involving fracture-induced discontinuity. This coupling model is applied for caprock integrity analysis for CO2 injection in a deep brine aquifer[29-30]. Chen discussed the implication of the X-FEM into ABAQUS via a new type of finite element.[31] However, to the best of our knowledge, there have been no studies on the direct coupling between X-FEM and EDFM for the fluid-driven fracture propagation simulation.

The objective of the present research is to construct a coupled numerical approach combining X-FEM and EDFM to simulate both 2D and 3D fluid-driven fracture propagation processes in the porous media. This study will also demonstrate the effectiveness of the simulation technique in predicting the complex processes. This paper is arranged as follows. Governing equations, numerical discretization approaches as well as the EDFM and X-FEM principles are briefly introduced in Section 2. In Section 3, key numerical techniques to couple these independent modules are described. In Section 4, several typical problems are simulated to validate the accuracy of our developed EDFM and X-FEM models. In Section 5, the coupled simulation is performed for both 2D and 3D fracture propagation problems. The matching of our numerical solutions with benchmark analytical solutions indicates this method produces correct results.

2. Governing equations and numerical formulations

This numerical study aims to understand the coupling between fluid flow and solid deformation during fluid-driven fracture propagations in porous media. These two physical processes have entirely different natures and behaviors, and thus they are characterized by different governing equations. Correspondingly, two different numerical schemes are adopted to solve these two sets of equations. The finite volume method (also known as the integral finite difference method) is preferred for discretizing fluid flow PDEs because it captures local conservations naturally, while the finite element method is adopted for solid mechanics because it is intuitive for the displacement compatibility.

The embedded discrete fracture method and the extended finite element method are two modeling techniques based on the finite volume method and the finite element method, respectively, for the fracture-related mechanics analysis. Both methods allow for the simulation related to fractures with structured grids. Thus, considerable flexibility is achieved by avoiding the construction of unstructured grids, which is quite challenging for complex three-dimensional fractures.

2.1. EDFM for fracture related fluid flow

The process of the fluid flow in porous and fractured media is gov-

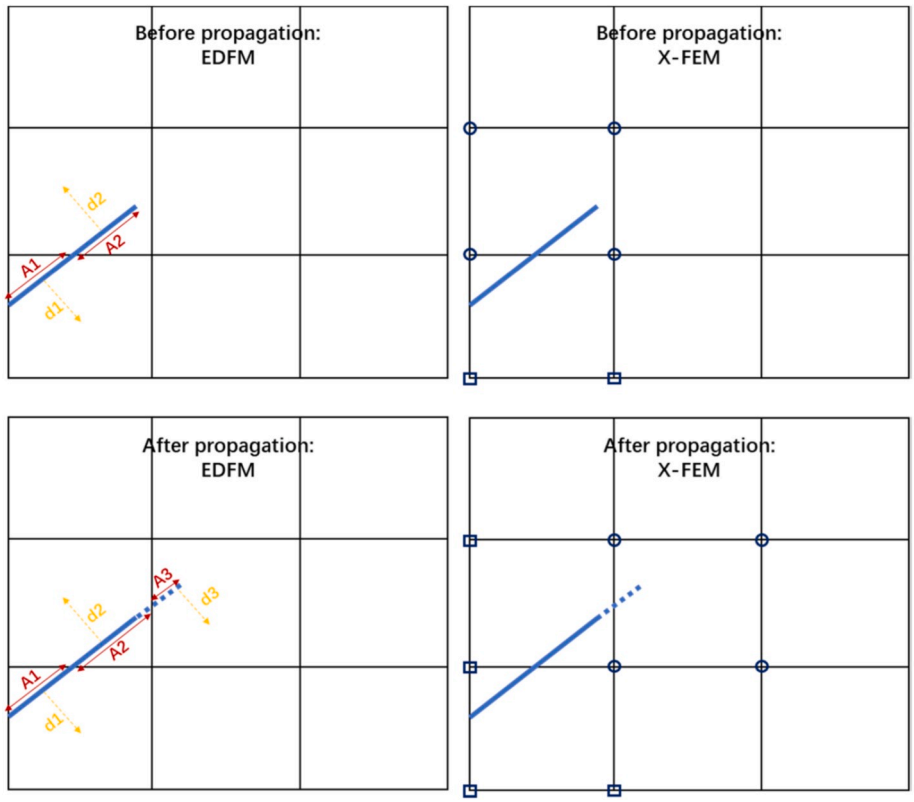

Fig. 2. Demonstration of EDFM and X-FEM for the fracture propagation.

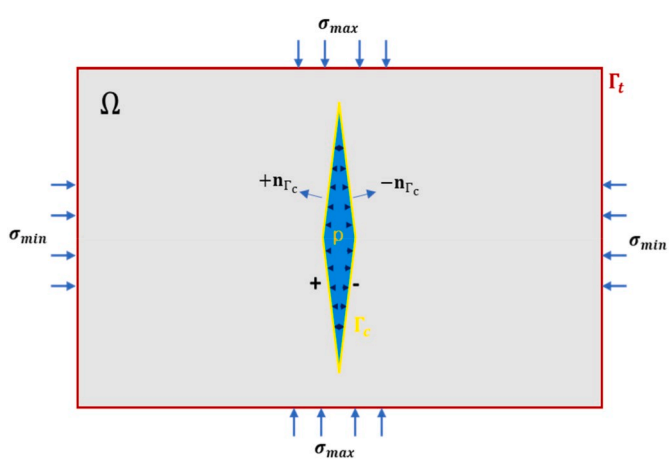

Fig. 3. Sketch diagram for a two-dimensional body.

erned by the mass conservation equation along with Darcy's law:

$$\frac{\partial}{\partial t}(\rho\varphi) + div(\rho\mathbf{v}) = q \tag{3}$$

where ρ is the fluid density; φ represents the porosity; v is the Darcy velocity, and q is the sink/source per unit volume per unit time.

With the integral finite difference method, the discrete nonlinear equations of Eq. (3) at node i are as follows[32,33]:

$$\frac{1}{\Delta t}\left[(f\rho V)_i^{n+1} - (f\rho V)_i^{n}\right] = \sum_{j\in\eta_i}\left(\frac{\rho}{\mu}\right)_{ij+1/2}^{n+1}\gamma_{ij}\left(\psi_j^{n+1} - \psi_i^{n+1}\right) + Q_i^{n+1} \tag{4}$$

where the superscript n and n+1 denote the previous time level and the current time level, respectively; V_i is the volume of element I; Δt is the time step size; η_i contains the set of neighboring elements (j) connecting to element i; subscript $ij+\frac{1}{2}$ denotes a proper averaging of properties at the interface between elements i and j; Q_i^{n+1} is the mass sink/source term at element i. γ_{ij} is the defined transmissivity of flow terms.

Table 1
Algorithm for the two-stage coupling between EDFM and X-FEM.

Algorithm: two stage coupling between EDFM and X-FEM	
1	Initialization
2	Time Step
2.1	Level-set function to capture fracture geometry for EDFM and XFEM
2.2	Solve fluid flow equations for fluid pressure with fracture width
2.3	Solver geomechanics equations for fracture width with fluid pressure
2.4	**if** (Step 2.2 and Step 2.3 NOT converge) then
2.4.1	**Goto** Step 2.2
2.5	**else**
2.5.1	**if** (Propagation criteria reached) **then**
2.5.1.1.	Update fracture geometry
2.5.1.2	**Goto** Step 2.1
2.5.2	**else**
2.5.2.1	Convergence reached in this time step
2.5.2.2	**Goto** Step 2

$$\gamma_{ij} = \frac{A_{ij}k_{ij+1/2}}{d_i + d_j} \tag{5}$$

where A_{ij} is the common interface area between two elements; d_i and d_j are distances from the element center (i and j) to the common interface. $k_{ij+1/2}$ is an averaged absolute permeability along this direction.

In the EDFM, fractures are conceptualized to be virtually embedded into nearby matrix grid blocks by treating them as a single or as several additional computational volume elements. The fracture thickness is only considered in the computational domain for fracture volume calculations, but not represented in the grid domain, because fracture thickness is several orders of magnitude smaller than the grid size. These

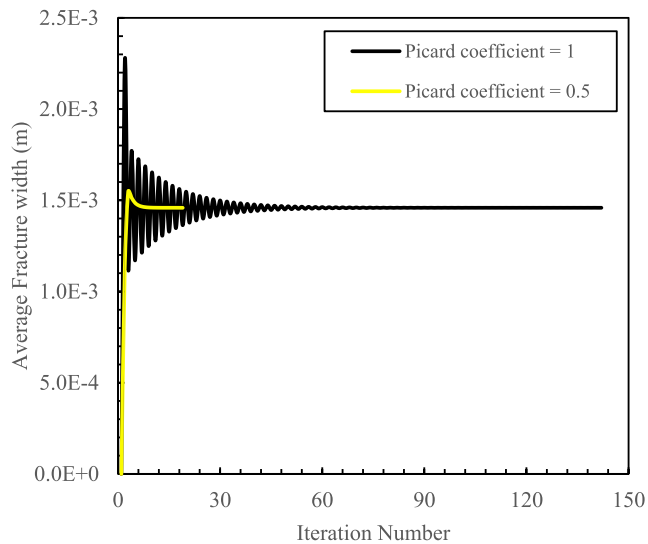

Fig. 4. Average fracture width as a function of the iteration number with Picard coefficient equals to 0.5 and 1.0.

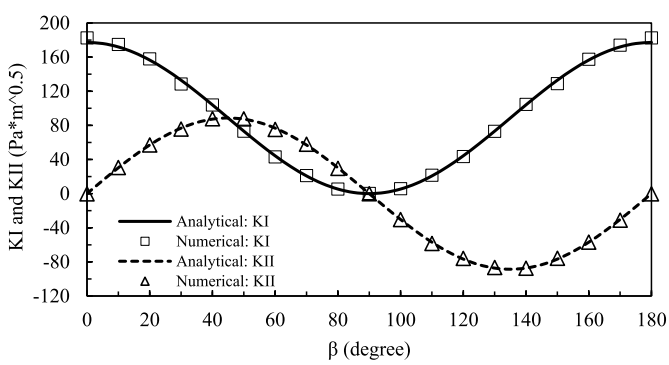

Fig. 5. Comparisons between numerical and analytical stress intensity factor.

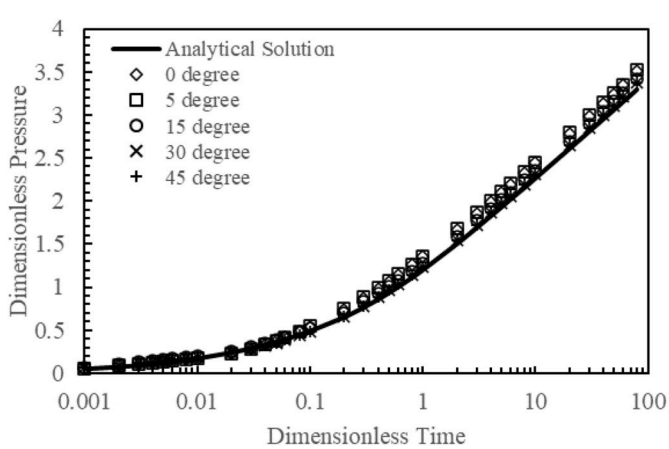

Fig. 6. Comparisons between numerical and analytical dimensionless pressure.

fracture volume elements connect to nearby matrix elements as well as connecting to adjacent fracture elements. Such connection information can be directly obtained through geometric processes, which calculate two critical parameters: the fracture-matrix contacting area and the average distance. In our previous work, we described a general geometrical calculation algorithm for complicated 3D fractures, proved this approach is accurate to handle steady and pseudo-steady state flow, and validated the EDFM approach by several numerical experiments.[21] Like the transmissivity term connecting two neighbor matrix elements (Eq. (5)), the fracture-index FI_i connecting the computational fracture volume and its local matrix computation volume is defined as:

$$\mathrm{FI_i} = \frac{\mathrm{A_i k_m}}{\mathrm{d_m + d_f}} \tag{6}$$

where A_i is the common interface area between the intersected block and the fracture; d_m and d_f are distances from the matrix grid block and the fracture to this interface according to EDFM assumptions.

2.2. X-FEM for fracture related solid deformation

The weak form of the stress equilibrium equation provides us with the principle of virtual displacements:

$$\int_V \bar{\varepsilon}^T \boldsymbol{\sigma} dV = \int_{\Gamma_t} \overline{\boldsymbol{U}}^{tT} \boldsymbol{f}^t \, d\Gamma_t + \int_{\Gamma_c} \overline{\boldsymbol{U}}^{cT} \boldsymbol{f}^c \, d\Gamma_c \tag{7}$$

where $\bar{\varepsilon}$, $\overline{\boldsymbol{U}}^t$ and $\overline{\boldsymbol{U}}^c$ are the virtual strain, virtual external boundary displacements, and virtual internal displacements at specific concentrated points, respectively; $\boldsymbol{f}^t$ and $\boldsymbol{f}^c$ are forces on boundaries; Γ_t and Γ_c are outer and internal boundaries for this object;

Rewrite Eq. (7) as a sum of integrations over all elements and substitute the strain-displacement, strain-stress relations into the equation,[12] we have

$$\boldsymbol{KU} = \boldsymbol{R} \tag{8}$$

where

$$\boldsymbol{K} = \sum_m \int_{V^{(m)}} \boldsymbol{B}^{(m)T} \boldsymbol{C}^{(m)} \boldsymbol{B}^{(m)} dV^{(m)} \tag{9}$$

$$\boldsymbol{R} = \sum_m \int_{\Gamma_c^{(m)}} \boldsymbol{h}^{c^{(m)T}} \boldsymbol{f}^{c(m)} d\Gamma_c^{(m)} + \sum_m \int_{\Gamma_t^{(m)}} \boldsymbol{h}^{t^{(m)T}} \boldsymbol{f}^{t(m)} d\Gamma_t^{(m)} \tag{10}$$

In Eq. (8), $\boldsymbol{K}$ is the global stiffness matrix; $\boldsymbol{R}$ is the residual vector related boundary conditions. $\boldsymbol{B}^{(m)}$ is the strain-displacement matrix for the element m, $\boldsymbol{C}^{(m)}$ is the stiffness matrix, and $\boldsymbol{h}^{(m)}$ is the displacement interpolation matrix.

In the X-FEM method, in addition to local element nodes according to the finite element method, the near fracture area is enriched by incorporating both discontinuous fields and the near-tip asymptotic fields.[22,23] The discretized displacement can be expressed as follows:

$$\mathrm{u}\left(\mathrm{x}\right) = \sum_{\mathrm{i}\in\mathrm{I}} \mathrm{u_i h_i} + \sum_{\mathrm{j}\in\mathrm{J}} \mathrm{b_j h_j H(x)} + \sum_{\mathrm{k}\in\mathrm{K}} \mathrm{h_k} \left(\sum_{\mathrm{l}=1}^{4} \mathrm{c_k^l F_l(x)} \right) \tag{11}$$

where u(x) is the displacement at the location x; The set I consists of local element nodes; The set K includes those nodes of which the closure support the crack front, and the set J is the set of nodes which support crack and do not belong to K. The vector $\mathrm{u_i}$, $\mathrm{b_j}$ and $\mathrm{c_k^l}$ are the displacement at nodes i, j and k, respectively; h is the displacement interpolation function; $H(x)$ is the discontinuous Heaviside function:

$$\mathrm{H(x)} = \begin{cases} -1 & \text{if } \mathrm{x} > 0 \\ +1 & \text{if } \mathrm{x} < 0 \end{cases} \tag{12}$$

$F_l(x)$ is the asymptotic crack tip functions based on the asymptotic features of the displacement field at the crack tip:

$$\mathrm{F_l(x)} = \left\{ \sqrt{\mathrm{r}} \sin\left(\frac{\theta}{2}\right), \sqrt{\mathrm{r}} \cos\left(\frac{\theta}{2}\right), \sqrt{\mathrm{r}} \sin\left(\frac{\theta}{2}\right) \sin(\theta), \sqrt{\mathrm{r}} \cos\left(\frac{\theta}{2}\right) \sin(\theta) \right\} \tag{13}$$

where (r, θ) are the local polar coordinates at the tip.

Fig. 2 plots a 2D fracture before and after growth, associated with

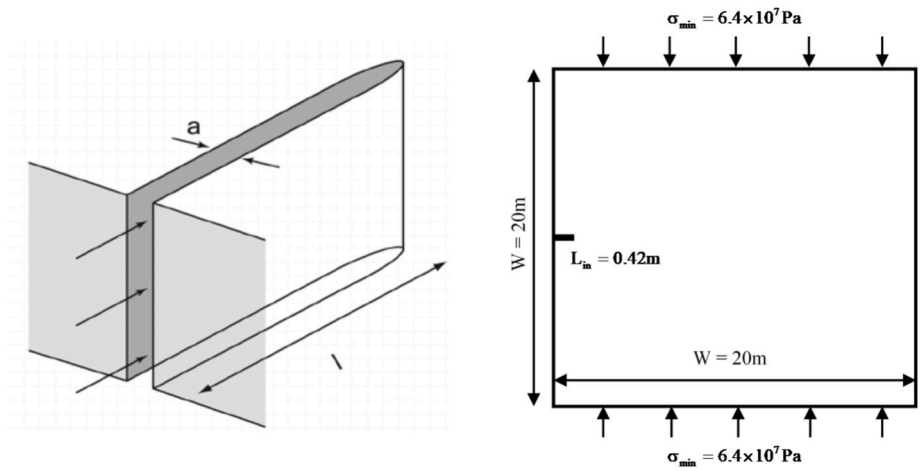

Fig. 7. Illustration of a KGD model (left) and its numerical setup in this study (right).

enrichment nodes for X-FEM and fluid-matrix flow connections for the EDFM. Two types of enrichment DOFs in X-FEM are demonstrated with black squares and black circles. The connection between the matrix grid block and the embedded fracture element in EDFM is represented by the contact area and distance.

3. The coupling principles

Strong fluid-solid coupling mechanics make the simulation of fluid-driven fracture propagation processes quite challenging. At least three physical processes (fluid flow, solid deformation, and fracture growth) and five relationships need to be considered[1]: (1) solid deformation changes the width of fractures and thus affects the effective fracture permeability as well as the fracture volume; (2) fluid flow induces solid deformation by the hydraulic loadings on crack surfaces; (3) fracture propagates when the stress state near the fracture tip meets the propagation criterion; (4) the growth of fractures cause the redistribution of the stress and strain fields, and (5) fluid flow is affected by the fracture growth since fractures provide a high-conductivity pathway. In this section, we describe physical explanations and mathematical equations on how to link these independent modules in detail. The link from fluid flow to solid deformation treats the fluid pressure force on the fracture surface as an internal boundary. The converse link takes the calculated fracture widths and corrects fracture permeability and the fracture volume. The geomechanics effect in the porous media caused by the change of pore pressure is not included in this study; one can refer to other literature for this part.[34,35]

3.1. Solid deformation on fluid flow

Solid deformation affects fluid flow by changing fracture widths, which determines the fracture permeability as well as the fracture volume. The crack opening displacement, as shown in Fig. 3, equals to the difference between two internal displacements on both sides of the fracture:

$$\boldsymbol{w} = \overline{\boldsymbol{U}}^{c+} - \overline{\boldsymbol{U}}^{c-} \tag{14}$$

Each internal displacement can be discretized as a linear combination of node displacements. Thus, the crack opening displacement can be obtained from the node displacement vector. This expression can be further simplified considering only the Heaviside function and the first asymptotic crack tip function in Eq. (11) are discontinuous across the fracture face.

$$\begin{aligned} \boldsymbol{w} &= \left\{ \sum_{i\in I} \mathbf{u}_i h_i^+ + \sum_{j\in J} \mathbf{b}_j h_j^+ H(\mathbf{x}^+) + \sum_{k\in K} h_k^+ \left[\sum_{l=1}^{4} \mathbf{c}_k^l F_l(\mathbf{x}^+) \right] \right\} \\ &\quad - \left\{ \sum_{i\in I} \mathbf{u}_i h_i^- + \sum_{j\in J} \mathbf{b}_j h_j^- H(\mathbf{x}^-) + \sum_{k\in K} h_k^- \left[\sum_{l=1}^{4} \mathbf{c}_k^l F_l(\mathbf{x}^-) \right] \right\} \\ &= 2\sum_{j\in J} \mathbf{b}_j h_j^+ H(\mathbf{x}^+) + 2\sum_{k\in K} h_k^+ \mathbf{c}_k^1 \sqrt{r} \end{aligned} \tag{15}$$

For a given fracture segment, its aperture is the length of the displacement:

$$\mathrm{w_f} = |\mathrm{w}| \tag{16}$$

The fracture aperture determines the fracture permeability according to the cubic law:

$$\mathrm{k_f} = \frac{\mathrm{w_f^2}}{12} \tag{17}$$

The volume of fracture element, as shown in Eq. (4), is related to the width by assuming local width variance in one grid block is negligible:

$$\mathrm{V_f} = \mathrm{w_f l_f h_f} \tag{18}$$

where l_f and h_f are the length and height of the fracture element, respectively.

3.2. Fluid flow on solid deformation

Fluid flow induces solid deformation by the hydraulic loading acting on crack surfaces. As shown in Fig. 3, the linear elastic body, which contains fractures filled with fluids, subjects to forces from fluids on crack surfaces. This internal boundary condition can be described as:

$$\sigma = \mathrm{p_f n_{\Gamma_c}} \quad \text{on } \Gamma_c \tag{19}$$

where σ is the stress vector; $\mathrm{p_f}$ is the fluid pressure in scalar form; Γ_c denotes this inner boundary by fractures; and $\mathrm{n_{\Gamma_c}}$ is the normal vector of this boundary.

In the weak form of stress equilibrium, this boundary condition appears in the residual part:

$$\int_{\Gamma_c} \overline{\mathrm{U}}^{c\mathrm{T}} \left(\mathrm{p_f n_{\Gamma_c}}\right) \mathrm{d}\Gamma_c = \int_{\Gamma_c^+} \overline{\mathrm{U}}^{c+\mathrm{T}} \left(\mathrm{p_f n_{\Gamma_c^+}}\right) \mathrm{d}\Gamma_c^+ + \int_{\Gamma_c^-} \overline{\mathrm{U}}^{c-\mathrm{T}} \left(\mathrm{p_f n_{\Gamma_c^-}}\right) \mathrm{d}\Gamma_c^- \tag{20}$$

where Γ_c^+ and Γ_c^- are two fracture faces; $\mathrm{n_{\Gamma_c^+}}$ and $\mathrm{n_{\Gamma_c^-}}$ are their associated normal vector pointing outside of the fracture. Since the angle between two fracture faces is close to zero, these two normal vectors can be approximated in opposite directions.

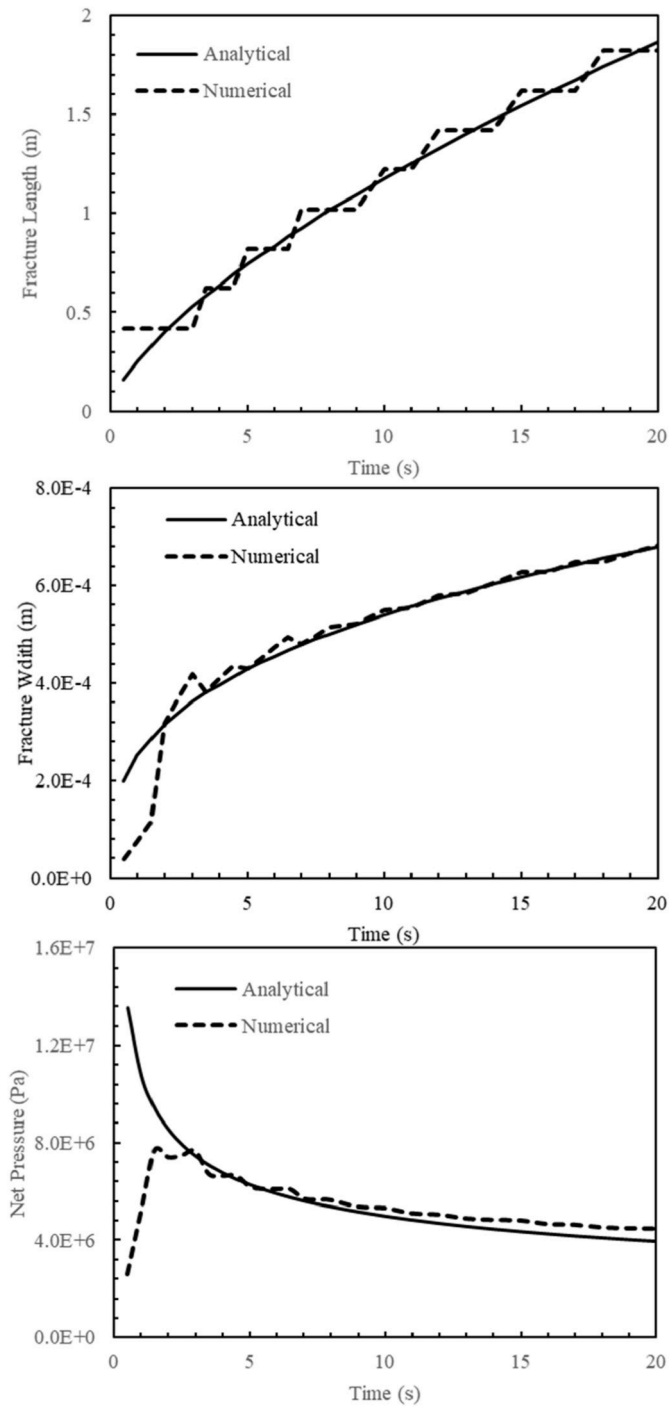

Fig. 8. Comparisons between numerical results and KGD analytical results. From up to bottom are the fracture length, fracture width at the inlet and the net pressure at the inlet.

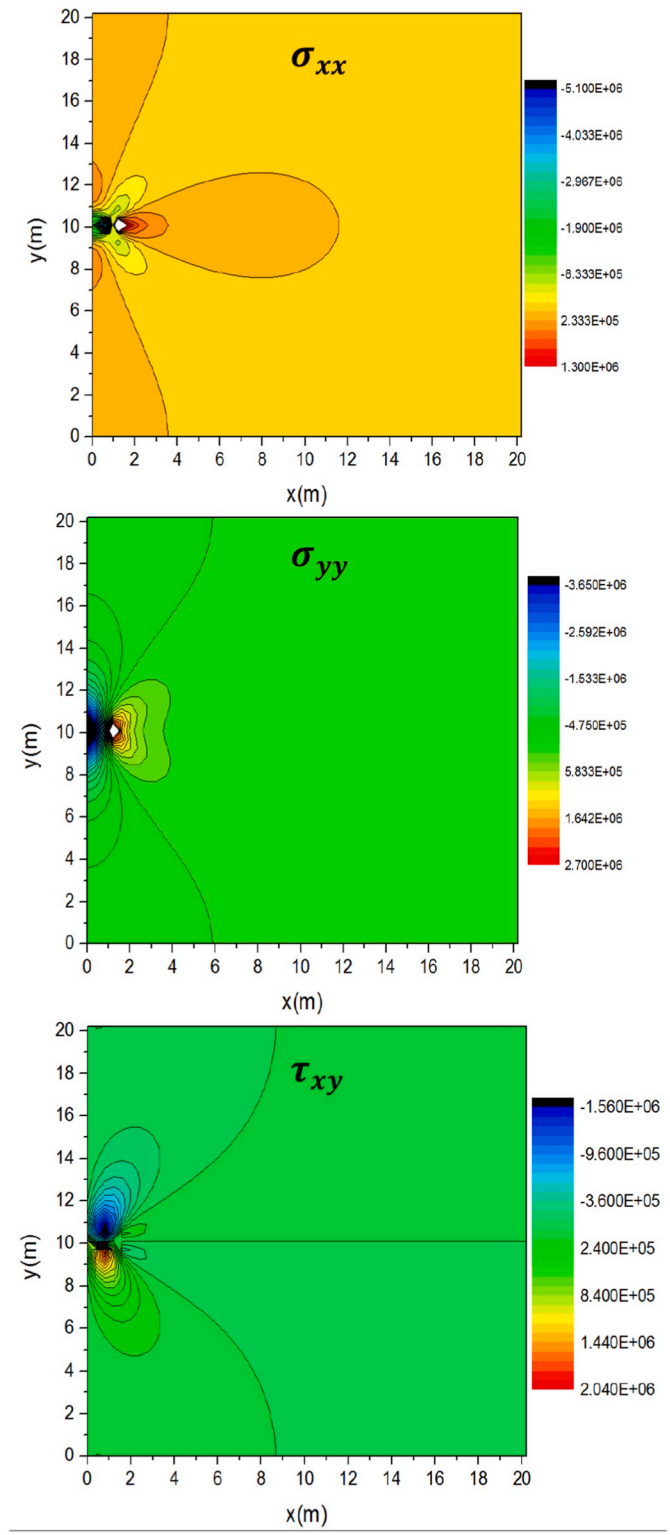

Fig. 9. Stress contour when the fracture length is 1.2 m. From top to bottom are the normal stress in the x-direction, the normal stress in the y-direction and shear stress.

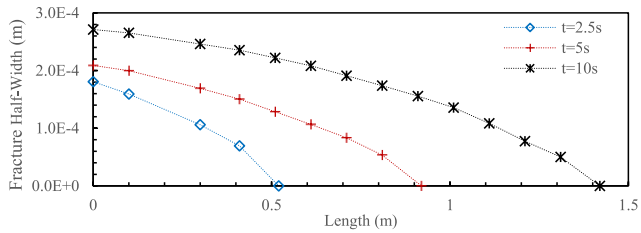

Fig. 10. Fracture geometry (half-width vs. length) at an injection time of 2.5s, 5s, and 10s.

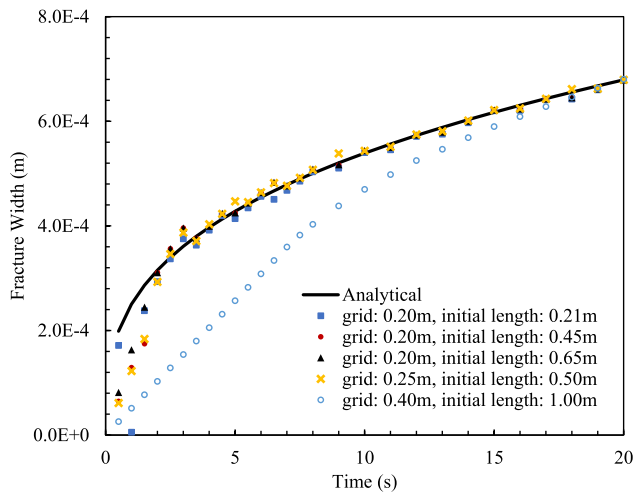

Fig. 11. Sensitivity analysis of the simulation results on grid size and initial fracture.

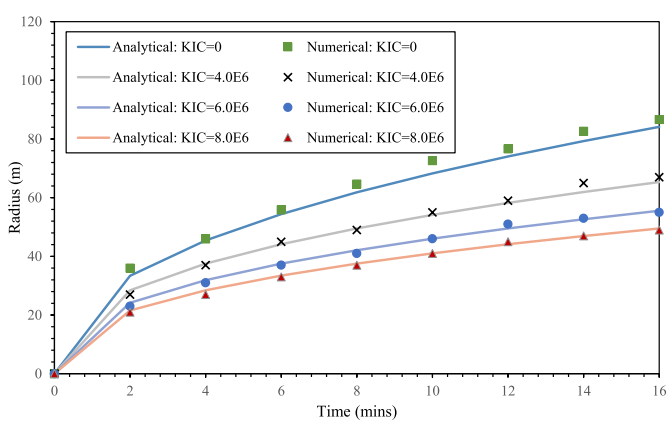

Fig. 12. Comparisons of the propagated fracture radius vs time between the analytical solution and the numerical solution with various fracture toughness.

$$\mathrm{n}_{\Gamma_c^+} \approx -\mathrm{n}_{\Gamma_c^-} \tag{21}$$

Substitute Eq. (14), Eq. (15) and Eq. (21) into Eq. (20), we have:

$$\int_{\Gamma_c^+} \overline{\boldsymbol{U}}^{c+T}\left(\mathrm{p_f}\mathbf{n}_{\Gamma_c^+}\right) d\Gamma_c^+ + \int_{\Gamma_c^-} \overline{\boldsymbol{U}}^{c-T}\left(\mathrm{p_f}\mathbf{n}_{\Gamma_c^-}\right) d\Gamma_c^- = \int_{\Gamma_c^+} \left(\overline{\boldsymbol{U}}^{c+T} - \overline{\boldsymbol{U}}^{c-T}\right)\left(\mathrm{p_f}\mathbf{n}_{\Gamma_c^+}\right) d\Gamma_c^+ = \int_{\Gamma_c^+} \left(2\sum_{j\in J}\mathbf{b}_j h_j^+ H(\mathbf{x}^+) + 2\sum_{k\in K} h_k^+ \mathbf{c}_k^1 \sqrt{r}\right)\left(\mathrm{p_f}\mathbf{n}_{\Gamma_c^+}\right) d\Gamma_c^+ \tag{22}$$

The equation above indicates the pressure force acting on the fracture surface can be transferred to the force acting on element nodes, which can be incorporated directly into the $\boldsymbol{R}$ matrix in Eq. (8). In this way, the effect of fluid flow on solid deformation is captured.

3.3. Solid deformation on fracture propagation

According to the theory of linear elastic fracture mechanics, a fracture can propagate if the stress intensity factor exceeds the fracture toughness. In this study, we use the maximum circumferential stress criterion for two-dimensional scenarios.[36,37] The fracture can grow if the following condition is met:

$$\mathrm{K}_{\theta_c} = \cos\frac{\theta_c}{2}\left(\mathrm{K_I}\cos^2\frac{\theta_c}{2} - \frac{3}{2}\mathrm{K_{II}}\sin\theta_c\right) \geq \mathrm{K_{IC}} \tag{23}$$

where K_{θ_c} is the maximum circumferential stress; $\mathrm{K_{IC}}$ is the fracture toughness, which is a property of the material; θ_c is the direction of fracture propagation:

$$\theta_c = 2\tan^{-1}\frac{1}{4}\left[\frac{\mathrm{K_I}}{\mathrm{K_{II}}} - \mathrm{sign}\,(\mathrm{K_{II}})\sqrt{\left(\frac{\mathrm{K_I}}{\mathrm{K_{II}}}\right)^2 + 8}\right] \tag{24}$$

In Eq. (23) and Eq. (24), $\mathrm{K_I}$ and $\mathrm{K_{II}}$ are the mode I and mode II stress intensity factors, which are defined as:

$$\mathrm{K_I} = \lim_{r\to 0}\sqrt{2\pi r}\,\sigma_{xx}(r,0) \tag{25}$$

$$\mathrm{K_{II}} = \lim_{r\to 0}\sqrt{2\pi r}\,\sigma_{xy}(r,0) \tag{26}$$

where σ_{xx} and σ_{xy} are the normal stress in the x-direction and the shear stress, respectively; r denotes the distance to the fracture tip. The length of crack growth can be correlated with the stress intensity factor as well according to Paris' law.

For 3D cases, the mode I stress intensity factor at the fracture tip can be calculated as (Yew and Weng 2014)

$$\mathrm{K_I} = \frac{\mathrm{E}}{8(1+\nu)(1-\nu)}\left(\frac{2\pi}{r}\right)^{1/2} \mathrm{w}(r) \tag{27}$$

3.4. Fracture propagation on solid deformation and fluid flow

The growth of fractures changes solid- and fluid-mechanical behaviors of the system, which are captured by the X-FEM and the EDFM without remeshing. The fracture path can be obtained explicitly by a set of discrete points or implicitly via the level-set method. In X-FEM, as indicated in Eq. (11), another two sets of degrees of freedom (DOF) are introduced for fractures. Their associated enrichment functions depend on the fracture path, which can be obtained directly through the geometric calculation. With the growth of fracture, the number of DOFs as well as their associated enrichment functions change correspondingly (Fig. 2). Ultimately, the global stiffness matrix (matrix **K** in Eq. (8)) is reconstructed. In the EDFM, the new fracture segment is represented by the addition of one or one assemblage of computational volume elements. Critical parameters for this incorporation are the contacting area and the average distance, which can also be geometrically obtained given the fracture path.

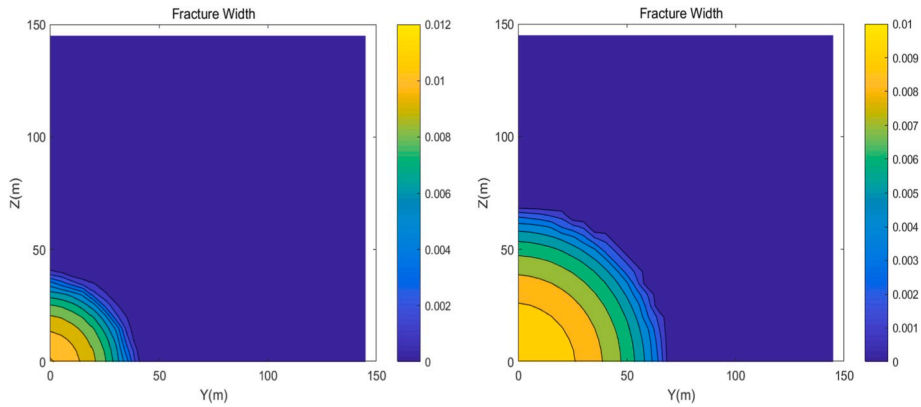

Fig. 13. Simulated fracture width distributions at 6 min and 16 min.

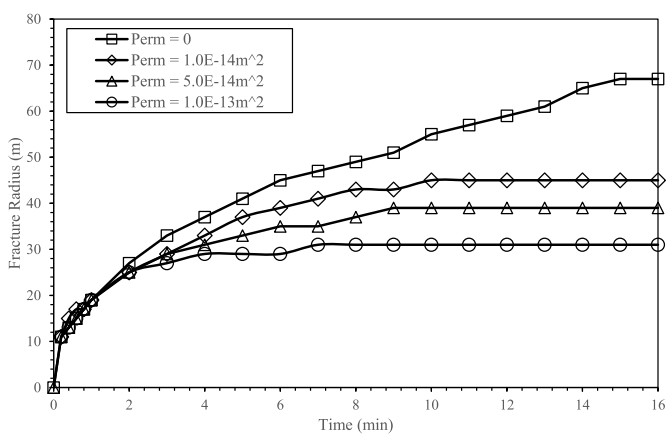

Fig. 14. Simulated fracture radius vs. time with various reservoir permeabilities.

3.5. Numerical coupling procedures

Three different routines are developed adequately: (1) modeling fluid flow in porous media with fractures based on the EDFM; (2) modeling solid deformation with fractures based on the X-FEM; and (3) determining if fracture propagates (if yes, calculating propagation length and directions). These three strongly interacted modules are coupled in two stages, as demonstrated in Table 1 by two loops. The goal of this two-stage coupling is obtaining a multi-physics field which satisfies all physics discussed above. This multi-physics field combines pressure field, stress field, and fracture geometry.

The iterative coupling method is selected for the coupling between fluid flow and solid deformation in the inner loop. Fluid flow variables and geomechanics variables are solved separately and sequentially by corresponding routines, and the coupling terms are interacted on at each time step. Data transfer between these two routines is described in sections above. The iterative coupling procedure is repeated until a satisfactory convergent fracture width is obtained. The criterion of convergence is

$$\max\left(\frac{\left|w^{n}_{k+1,i}-w^{n}_{k,i}\right|}{w^{n}_{k+1,i}}\right) < \varepsilon \tag{28}$$

where ε is an assigned tolerance.

Note that this iterative method uses an initial guess to generate successive approximations to the solution. For the first time step, this initial estimate is obtained by pre-running the iterative coupling with an infinite fracture permeability. For the following time steps, the converged result at the last time step is used. The Picard iteration technique is adopted to mitigate numerical oscillations and accelerate the convergence rate.

$$w^{(n)}_{k+1} = \alpha F\left(w^{(n)}_{k}\right) + (1-\alpha) w^{(n)}_{k}, \quad 0 < \alpha \le 1 \tag{29}$$

where α is the Picard coefficient; $w^{(n)}_{k}$ is the fracture width in the kth iteration during the nth time step; $F(w^{(n)}_{k})$ is the calculated fracture width after one loop of calculations based on $w^{(n)}_{k}$; and $w^{(n)}_{k+1}$ is the updated fracture width for the next iteration. For a 2D numerical test, the iteration number reduces from 142 to 19 by changing the Picard coefficient from 1.0 to 0.5 (Fig. 4).

Once the iteration between these two modules is converged, the stress intensity factor is calculated and compared with the fracture toughness to determine if the fracture propagates (Eq. (23)). If the fracture propagation criterion is not met, which means the fracture in this condition is stable, the coupling convergence among these three modules is achieved. Otherwise, the fracture propagation fracture geometry is updated for the next large-loop iteration (Table 1).

4. Validations

In this section, two numerical experiments are conducted to evaluate the accuracy of our developed X-FEM and EDFM codes. The in-house program used in this paper is written in MATLAB. The X-FEM codes are developed based on an open-source 2D MATLAB X-FEM codes.[38] The validation benchmarks chosen for these two tests are analytical solutions.

4.1. Solid deformation model validations

An angled center crack is put inside a plate which is subjected to a far-field uniaxial stress. The plate dimensions are five times larger than the crack length to approximate the infinite setting. The exact stress intensify factors for the infinite plate is given[39]:

$$K_I = \sigma\sqrt{\frac{\pi L}{2}}\cos^2(\beta) \tag{30}$$

$$K_{II} = \sigma\sqrt{\frac{\pi L}{2}}\sin(\beta)\cos(\beta) \tag{31}$$

A series of numerical experiments are conducted by rotating the center crack. Fig. 5 shows numerically calculated stress intensity factors have a good agreement with the analytical solution for the entire range of β.

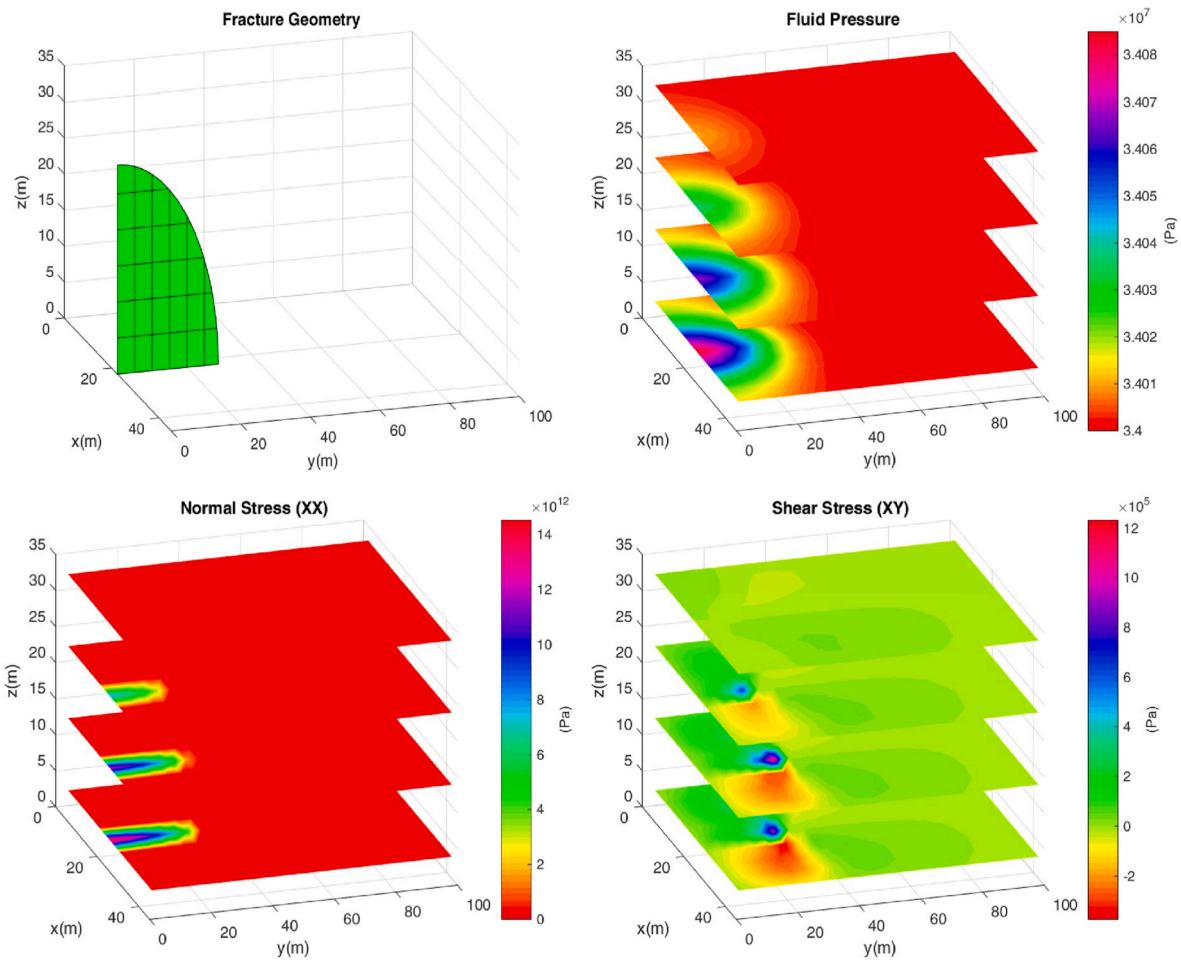

Fig. 15. Simulated fracture geometry, fluid pressure profile and stress profiles.

4.2. Fluid flow model validations

An angled center crack is put inside a closed-boundary 2D reservoir with the unit thickness. Fluid is produced at a constant rate from the fracture center. Gringarten et al. give the general analytical solution of the well pressure with a "uniform flux" or "infinite-conductivity" vertical fracture[40]:

$$p_D\left(t_{Dxf}, |x_D| < 1\right) = \frac{\sqrt{\pi t_{Dxf}}}{2}\left[erf\left(\frac{1-x_D}{2\sqrt{t_{Dxf}}}\right) + erf\left(\frac{1+x_D}{2\sqrt{t_{Dxf}}}\right)\right] - \frac{1-x_D}{4}Ei\left[-\frac{(1-x_D)^2}{4t_{Dxf}}\right] - \frac{1+x_D}{4}Ei\left[-\frac{(1+x_D)^2}{4t_{Dxf}}\right] \tag{32}$$

where erf and Ei denote the error function and exponential integral functions, respectively; $x_D = 0$ for the uniform flux case, and $x_D = 0.732$ for the infinite conductivity vertical fracture case. Simulations with various fracture angles are conducted. Since the reservoir can be approximated as the infinite set, the pressure data at the production point with various fracture angles keep the same. Fig. 6 plots analytical solutions of the dimensionless pressure at the fracture center as well as numerical solutions with various fracture angles. The good agreement verifies our numerical implementations about the EDFM is correct.

5. Numerical results

The developed coupling method is here applied to two fracture propagation problems in two dimensions and three dimensions, respectively. Models designed for these two problems are based on the classical KGD model and the penny-shaped fracture model. The primary objective of these two examples is to demonstrate the capacity of our developed numerical coupling approach in accurately simulating the complex multiphysics in the fracture propagation process. Note that though fracture geometries in these two illustrative examples are relatively simple, the coupling approach is applicable for complicated-geometry cases because both X-FEM and EDFM can handle fractures with complicated geometries.

5.1. Two dimensional KGD model

This section simulates a 2D hydraulic fracture propagation problem. The model designed is based on the classical Khristianovic-Geertsma-de Klerk (KGD) model. As demonstrated in Fig. 7, it composes only one layer of linear elastic medium with Young's modulus of 4.14×10^{10} Pa and the Poisson's ratio of 0.20. The thickness of the formation layer is 1.0 m. Its minimum stress is 6.4×10^7 Pa. Incompressible Newtonian fluid (with the viscosity of 1.00 $Pa{\cdot}s$) is injected at a constant rate of $5.0 \times 10^{-5} m^3/s$ for 20 s, which initializes and propagates the hydraulic fracture. Both the fracture toughness and the formation permeability are set to be zero following assumptions in the classical KGD model.

Fig. 8 presents comparisons of fracture half-length, fracture width at the wellbore, and net pressure, respectively, which are calculated from numerical and analytical solutions. The analytical solution for the above problem can be found from the textbook.[41] These comparisons indicate that numerical results are in good agreements with the analytical solution for this problem. The discrepancy in the early time is because the fracture is assumed to grow from an initial length of 0.42 m instead of

zero. The difference afterward is caused by grid resolutions (cell size) in the numerical approach. Note that the numerical method in this study simulates fracture propagation with a single wing. The contour of the normal stress in the x-direction, the normal stress in the y-direction and the shear stress when the fracture length is 1.21 m is plotted in Fig. 9. It can be seen that the stress concentration effect at the fracture tip is captured in the simulation result. Fracture half-width profiles at different injection time are shown in Fig. 10.

A series of numerical tests are then conducted by varying the grid size and initial fracture length to investigate their influence on simulated fracture geometry. Detailed input parameters, as well as simulated fracture inlet widths, are demonstrated in Fig. 11. For this problem, this coupling numerical algorithm can converge to the correct answer if the grid size and the initial fracture length are set up relatively conservatively. However, the accuracy cannot be unconditionally guaranteed if the initial set up is too deviated, as can be seen in the case with the grid size of 0.4 m and the initial length of 1.0 m

5.2. Three dimensional penny-shaped fracture model

The penny-shape fracture propagation problem involves an axisymmetric hydraulic fracture propagation in a 3D infinite elastic medium. In this problem, the formation of Young's modulus is 5.83×10^{10} Pa and the Poisson's ratio is 0.30. The formation initial reservoir pressure is 3.4×10^7 Pa, and the minimum stress is 6.4×10^7 Pa. Incompressible Newtonian fluid with the viscosity of 0.1 $Pa{\cdot}s$ is injected at the fracture center with a constant rate of $0.106m^3/s$. In the base case, the fracture toughness is $4.0 \times 10^6\ Pa\sqrt{m}$, and the formation permeability is zero. Six other cases with variational fracture toughness and formation permeabilities are also simulated to conduct the sensitivity analysis. The analytical solution considering both are not available, and only comparisons between the simulation results and analytical results for cases without fluid leak-off are presented.

Only a quarter of the fracture is simulated by considering symmetry in this problem. The fracture is positioned in the mid of the X-axis. This quarter-model has dimensions of $45m \times 150m \times 150m$ which contain 8100 elements. The size of each element is $5m \times 5m \times 5m$. The reservoir permeability is zero to model the impermeable rock condition as assumed in the analytical solution. If the fracture propagation criteria are met, the increase of fracture radius is set to be 2.0 m.

In addition to the base case, three other cases are simulated with different fracture toughness (0, $6.0 \times 10^6\ Pa\sqrt{m}$, and $8.0 \times\ 10^6\ Pa\sqrt{m}$). Both viscosity-dominated and toughness-dominated scenarios are covered in these four cases. Analytical solutions for the fracture radius of this penny-shaped fracture with viscosity-dominated ($K < 1$) regime and toughness-dominated regime ($K > 4$) can be referred in literature.[6]

Fig. 12 presents comparisons between the numerical solutions and analytical solutions about the fracture radius vs. time with various fracture toughness. It indicates from low toughness ($K_{IC} = 0$) to high ones ($K_{IC} = 8.0 \times 10^6\ Pa\sqrt{m}$), all results from the numerical approach are in good agreement with the analytical solutions. Simulated fracture width profiles for the base case at 6 min and 16 min are demonstrated in Fig. 13.

We also conducted a sensitivity analysis concerning the reservoir permeability. Three cases with various formation permeability ($1.0 \times 10^{-14}\ m^2$, $5.0 \times 10^{-14}\ m^2$ and $1.0 \times 10^{-13}\ m^2$) are simulated. Simulated fracture radius vs. time in these three cases are compared with the result of the base case, as shown in Fig. 14. It indicates that the loss of fluid into formations also governs the fracture extent, like the fracture toughness. The amount of this fluid loss is controlled by the fluid viscosity, formation permeability, fracture-matrix contact area, and the fracture-matrix pressure difference. For the highest permeability ($1.0 \times 10^{-13}\ m^2$) case, the fracture radius grows to 31 m with 7 min of fluid injections. This fracture growth stops afterward because a dynamic balance is reached between the fluid injection and the fluid loss into formations. With the decrease of formation permeability, this ultimate fracture radius increases and the time to reach this radius increases as well. One can expect this fracture radius regrows with enough injections when the formation pressure is increased to a value close to the fluid pressure in fractures. But this phenomenon is not observed in the time range of this simulation (16 min). For the case of zero permeability, the fracture keeps increasing with a gradually slowing down growth rate.

This coupling algorithm can calculate six stress components (three normal stresses and three shear stresses) and one fluid pressure with time. Here we show 3D contours of the simulated fluid pressure, xx-normal stress and xy-shear stress after 5 min of injections for the case with the permeability of $1.0 \times 10^{-13}m^2$ (Fig. 15). Results at four horizontal layers (z = 3 m, 13 m, 23 m and 33 m) are demonstrated. The simulated radius of the propagated fracture at this time is 29 m.

Fig. 15 demonstrates that this numerical algorithm captures different patterns and scopes for the fields of three coupling physics (fracture propagation, fluid flow and solid deformation) in this problem. Simulation results meet the qualitative expectation as well. The simulated fluid pressure contour cannot be described by the exact linear flow pattern because the time fluid leak-off begins at different fracture locations varies. A slight pressure depletion at the horizontal layer of z = 33 m is observed, although the fracture tip hasn't reached this height. This is because fluid flows in the vertical direction with pressure differences in the porous media. The stress concentration effect at the fracture tip, which is a key in the linear elastic fracture mechanics, can be observed in the xy-shear stress contour with different heights.

6. Summary

1. We present a coupled simulation strategy combining the embedded discrete fracture method and the extended finite element method to simulate the fluid-driven fracture propagation process in porous media. Key physics in this process includes three strong coupling mechanics: fluid flow in fractures and porous media, solid deformation with fractures, and fracture propagations can be captured through this numerical approach. Both EDFM and X-FEM avoid the cumbersome construction of unstructured grids to capture fracture paths for fracture-related fluid mechanics and solid mechanics. They also avoid the remeshing for the fracture growth.

2. Mathematical equations on how to link these independent modules as well as numerical techniques on how to accelerate the coupling convergence rate are discussed in detail. The link from fluid flow to solid deformation treats the fluid pressure force on the fracture surface as an internal boundary. The converse link takes the calculated fracture widths and corrects fracture permeability and the fracture volume. The growth of fracture path is calculated based on the stress field from the X-FEM simulation. This fracture growth, in turn, changes solid- and fluid-mechanical behaviors of the system, which are captured by the reconstruction of equations in EDFM and X-FEM.

3. The EDFM and X-FEM are validated via benchmark problems individually and then are coupled to simulate fracture propagation problems in two dimensions and in three dimensions. Simulated multi-physics fields meet understandings qualitatively, and simulated fracture parameters (length, width and net pressure) match with analytical solutions (KGD for 2D problems and Penny-shaped fracture model for 3D problems) quantitatively.

4. In this 3D demonstration example, because we assume the formation is homogeneous and isotropic, the fracture propagates following a penny shape, and thus the front shape can be controlled just by the radius. For more complicated 3D applications, tracking the 3D fracture surface and capturing the fracture paths, determining the direction and length of fracture growth are challenging and not covered in this work. Further development addressing these questions will enable this numerical tool for more complicated and practical engineering analysis.

Declaration of competing interest

The authors declare that they have no known competing financial interests or personal relationships that could have appeared to influence the work reported in this paper.

Acknowledgements

This work was supported in part by EMG Research Center in Petroleum Engineering Department at Colorado School of Mines; by CNPC USA; by Chuanqiong Drilling Engineering Company; and by Foundation CMG.

References

1 Shlyapobersky J. Energy analysis of hydraulic fracturing. In: *The 26th US Symposium on Rock Mechanics (USRMS)*. American Rock Mechanics Association; January 1985.
2 Zheltov Y, Khristianovic S. Formation of vertical fractures by means of highly viscous fluids. In: *Proc. 4th World Petroleum Congress, Rome*. vol. 2. June 1955:579–586.
3 Perkins TK, Kern LR. Widths of hydraulic fractures. *J Petrol Technol*. 1961;13(9):937–949.
4 Geertsma J, De Klerk F. A rapid method of predicting width and extent of hydraulically induced fractures. *J Petrol Technol*. 1969;21(12):1–571.
5 Detournay E. Fluid and solid singularities at the tip of a fluid-driven fracture. In: *IUTAM Symposium on Non-linear Singularities in Deformation and Flow*. Dordrecht: Springer; 1999:27–42.
6 Savitski AA, Detournay E. Propagation of a penny-shaped fluid-driven fracture in an impermeable rock: asymptotic solutions. *Int J Solid Struct*. 2002;39(26):6311–6337.
7 Clifton RJ, Abou-Sayed AS. A variational approach to the prediction of the three-dimensional geometry of hydraulic fractures. In: *SPE/DOE Low Permeability Gas Reservoirs Symposium*. Society of Petroleum Engineers; January 1981.
8 Gu H, Yew CH. Finite element solution of a boundary integral equation for mode I embedded three-dimensional fractures. *Int J Numer Methods Eng*. 1988;26(7):1525–1540.
9 Xu G, Ortiz M. A variational boundary integral method for the analysis of 3-D cracks of arbitrary geometry modelled as continuous distributions of dislocation loops. *Int J Numer Methods Eng*. 1993;36(21):3675–3701.
10 Bui HD. An integral equations method for solving the problem of a plane crack of arbitrary shape. *J Mech Phys Solid*. 1977;25(1):29–39.
11 Howard GC, Fast CR. Optimum fluid characteristics for fracture extension. In: *Drilling and Production Practice*. January: American Petroleum Institute; 1957.
12 Bathe KJ. *Finite Element Procedures*. Klaus-Jurgen Bathe; 2006.
13 Chan SK, Tuba IS, Wilson WK. On the finite element method in linear fracture mechanics. *Eng Fract Mech*. 1970;2(1):1–17.
14 Smith IM, Griffiths DV, Margetts L. *Programming the Finite Element Method*. John Wiley & Sons; 2003.
15 Salimzadeh S, Paluszny A, Zimmerman RW. Three-dimensional poroelastic effects during hydraulic fracturing in permeable rocks. *Int J Solid Struct*. 2017;108:153–163.
16 Karimi-Fard M, Durlofsky LJ, Aziz K. An efficient discrete fracture model applicable for general purpose reservoir simulators. In: *SPE Reservoir Simulation Symposium*. January: Society of Petroleum Engineers; 2003.
17 Kim JG, Deo MD. Finite element, discrete-fracture model for multiphase flow in porous media. *AIChE J*. 2000;46(6):1120–1130.
18 Lee SH, Lough MF, Jensen CL. Hierarchical modeling of flow in naturally fractured formations with multiple length scales. *Water Resour Res*. 2001;37(3):443–455.
19 Li L, Lee SH. Efficient field-scale simulation of black oil in a naturally fractured reservoir through discrete fracture networks and homogenized media. *SPE Reservoir Eval Eng*. 2008;11(4):750–758.
20 Moinfar A, Varavei A, Sepehrnoori K, Johns RT. Development of a coupled dual continuum and discrete fracture model for the simulation of unconventional reservoirs. In: *SPE Reservoir Simulation Symposium*. Society of Petroleum Engineers; 2013.
21 Wang C, Ran Q, Wu YS. Robust implementations of the 3D-EDFM algorithm for reservoir simulation with complicated hydraulic fractures. *J Petrol Sci Eng*. 2019;181:106229.
22 Moës N, Dolbow J, Belytschko T. A finite element method for crack growth without remeshing. *Int J Numer Methods Eng*. 1999;46(1):131–150.
23 Sukumar N, Chopp DL, Moës N, Belytschko T. Modeling holes and inclusions by level sets in the extended finite-element method. *Comput Methods Appl Mech Eng*. 2001;190(46-47):6183–6200.
24 Wang C, Winterfeld P, Johnston B, Wu YS. An embedded 3D fracture modeling approach for simulating fracture-dominated fluid flow and heat transfer in geothermal reservoirs. *Geothermics*. 2020;86:101831.
25 Hui MHR, Karimi-Fard M, Mallison B, Durlofsky LJ. A general modeling framework for simulating complex recovery processes in fractured reservoirs at different resolutions. *SPE J*. 2018;23(2):598–613.
26 Wang Z, Yu T, Bui TQ, et al. 3-D local mesh refinement XFEM with variable-node hexahedron elements for extraction of stress intensity factors of straight and curved planar cracks. *Comput Methods Appl Mech Eng*. 2017;313:375–405.
27 Agathos K, Ventura G, Chatzi E, Bordas SP. Stable 3D XFEM/vector level sets for non-planar 3D crack propagation and comparison of enrichment schemes. *Int J Numer Methods Eng*. 2018;113(2):252–276.
28 Lecampion B. An extended finite element method for hydraulic fracture problems. *Commun Numer Methods Eng*. 2009;25(2):121–133.
29 Pan PZ, Rutqvist J, Feng XT, Yan F. TOUGH–RDCA modeling of multiple fracture interactions in caprock during CO2 injection into a deep brine aquifer. *Comput Geosci*. 2014;65:24–36.
30 Pan PZ, Rutqvist J, Feng XT, Yan F. An approach for modeling rock discontinuous mechanical behavior under multiphase fluid flow conditions. *Rock Mech Rock Eng*. 2014;47(2):589–603.
31 Chen Z. An ABAQUS implementation of the XFEM for hydraulic fracture problems. In: *ISRM International Conference for Effective and Sustainable Hydraulic Fracturing*. International Society for Rock Mechanics and Rock Engineering; May 2013.
32 Wu YS. A virtual node method for handling well bore boundary conditions in modeling multiphase flow in porous and fractured media. *Water Resour Res*. 2000;36(3):807–814.
33 Pruess K, Oldenburg CM, Moridis GJ. *TOUGH2 User's Guide Version 2 (No. LBNL-43134)*. Berkeley, CA (United States): Lawrence Berkeley National Lab.(LBNL); 1999.
34 Rutqvist J, Wu YS, Tsang CF, Bodvarsson G. A modeling approach for analysis of coupled multiphase fluid flow, heat transfer, and deformation in fractured porous rock. *Int J Rock Mech Min Sci*. 2002;39(4):429–442.
35 Hu L, Winterfeld PH, Fakcharoenphol P, Wu YS. A novel fully-coupled flow and geomechanics model in enhanced geothermal reservoirs. *J Petrol Sci Eng*. 2013;107:1–11.
36 Shih CF, Asaro RJ. Elastic-plastic analysis of cracks on bimaterial interfaces: part I—small scale yielding. *J Appl Mech*. 1988;55(2):299–316.
37 Paris P, Erdogan F. A critical analysis of crack propagation laws. *J Basic Eng*. 1963;85(4):528–533.
38 Pais M, Kim NH, Davis T. Reanalysis of the extended finite element method for crack initiation and propagation. In: *51st AIAA/ASME/ASCE/AHS/ASC Structures, Structural Dynamics, and Materials Conference 18th AIAA/ASME/AHS Adaptive Structures Conference 12th*. 2010.
39 Tada H, Paris PC, Irwin GR, Tada H. *The Stress Analysis of Cracks Handbook*. vol. 130. New York: ASME press; 2000.
40 Gringarten AC, Ramey Jr HJ, Raghavan R. Unsteady-state pressure distributions created by a well with a single infinite-conductivity vertical fracture. *Soc Petrol Eng J*. 1974;14(4):347–360.
41 Yew CH, Weng X. *Mechanics of Hydraulic Fracturing*. Gulf Professional Publishing; 2014.